Microphysical precursor conditions leading to precipitation initiation in marine stratocumulus

By

Hannah E. Chandler

Submitted to the graduate degree program in Geography and Atmospheric Sciences and the Graduate Faculty of the University of Kansas in partial fulfillment of the requirements for the degree of Master of Science.

Chair: David B. Mechem

Nathaniel A. Brunsell

David A. Rahn

Date Defended: 9 December 2016

The thesis committee for Hannah Chandler

certifies that this is the approved version of the following thesis:

Microphysical precursor conditions leading to precipitation initiation in marine stratocumulus

Chair: David B. Mechem

Date Approved: 9 December 2016

Abstract

Although the classical model of how a population of cloud droplets grows to precipitation-sized drops through the condensation and coalescence processes is well accepted, it does not fully address the history of how nascent precipitation drops come about in warm clouds. A size-resolving (bin) large-eddy simulation (LES) model and a parcel trajectory model are used to investigate the dominant microphysical precursor conditions influencing precipitation initiation for a case of marine stratocumulus based on conditions sampled during the CAP-MBL field campaign in the eastern North Atlantic. Backward trajectories are then calculated beginning from ten regions of nascent precipitation to analyze the precursor conditions of precipitation onset. A suite of backward trajectories is also calculated from ten null cases originating in regions that do not form drizzle.

The backward trajectories originating in nascent drizzle regions exhibit larger mean cloud droplet radius (r_v) relative to the null cases, as would be expected since larger cloud droplets tend to preferentially form drizzle. These nascent drizzle cases experience anomalously low droplet concentration (N_c) along the trajectory path, relative to the null cases, but also low values of cloud-water mixing ratio (q_c). These results indicate the most surprising aspect of our study, specifically that the larger values of mean volume radius (r_v) are driven, not by large cloud liquid water contents (q_c), but rather by small values of cloud droplet concentration (N_c). These findings suggest that new regions of drizzle are associated with parcels that previously participated in the drizzle process.

Acknowledgements

I want to thank my advisor Dr. David Mechem for all of the hard work and support he has offered on my research and throughout my time here at the University of Kansas. I would like to thank my committee members Dr. Nathaniel Brunsell and Dr. David Rahn for their invaluable time and input into my research. Thank you to my collaborators Drs. Ann Fridlind and Andrew Ackerman from NASA Goddard Institute for Space Science for supplying model case specifications. Thank you to the Department of Energy Office of Science for funding my research with grant DE-SC0006736. A big thank you to all of my fellow graduate students, past and present, for all of your insight and emotional support throughout the past two and a half years. Finally, I would like to thank Kate Cooley, my parents Brent and Shelley Chandler, my sister Alyssa Chandler, Emily Knudsen, Anna Chasse, the Cooley clan, and the rest of my wonderful extended family and friends for all of your continued encouragement and support throughout my entire educational career. I would never had made it to this point without all of you.

Table of Contents

Chapter 1

Introduction

Stratocumulus clouds are the most dominant cloud type on Earth, covering approximately one-fifth of Earth's surface in the annual mean (Warren et al. 1986; Hahn and Warren 2007) and constituting a significant component in the earth's radiation budget (Stephens and Greenwald 1991). Stratocumulus clouds predominantly reside over the ocean and are most commonly associated with the downward branches of the Hadley and Walker circulations over the eastern portions of the subtropical and midlatitude oceans where subsidence and cool sea surface temperatures prevail (Klein and Hartmann 1993). The prevalence of stratocumulus over the oceans and their impact on the global radiation budget have motivated research aimed at understanding marine stratocumulus behavior and sensitivity to climate perturbations.

Precipitation plays a role in governing stratocumulus properties. Evaporative cooling from drizzle stabilizes the subcloud layer, which reduces turbulent kinetic energy (TKE) production (Stevens et al. 1998). This stabilization promotes the decoupling of the boundary layer circulation into distinct cloud- and subcloud-layers and can inhibit moisture flux from the surface into the cloud layer, leading to a thinning of the cloud with time (Ackerman et al. 1993; Stevens et al. 1998). Drizzle is a sink for liquid water and for sufficient drizzle rates can limit cloud liquid water path (LWP; Albrecht 1989). On the other hand, drizzle typically decreases entrainment and consequently cloud thinning from entrainment-drying (Stevens et al. 1998) which may lead to thicker PBL clouds, relative to a nonprecipitating cloud. Which of these competing mechanisms dominates depends in

part on drizzle magnitude, inversion strength, and free-tropospheric humidity (Ackerman et al. 2004, 2009).

The classical model of liquid-water precipitation formation and growth, termed the warm-rain process, begins with cloud droplets first forming through nucleation on cloud condensation nuclei (CCN). These cloud droplets then grow, and through condensation and collision-coalescence, result in drizzle-sized droplets. However, it is not fully understood how cloud droplets initiate drizzle in warm clouds since droplets cannot grow via condensation to drizzle sizes fast enough compared to observed timescales of drizzle formation, and collision efficiencies are small for small droplets (Beard and Ochs 1993). This dilemma, typically referred to as the coalescence bottleneck, remains a central topic of warm-rain microphysics research. Current research projects focus on four principal explanations to resolve the dilemma: turbulence enhancement, entrainment enhancement, growth on giant CCN (GCCN), and dynamic and thermodynamic forcings.

Precipitation initiation is influenced by cloud drop properties (and by extension, CCN properties) within a cloud. Multiple studies have found the size of cloud droplets strongly influences the formation and rate of drizzle in stratocumulus clouds (e.g. Beard and Ochs 1993; Ackerman et al. 1995; Khairoutdinov and Kogan 2000; Jiang et al. 2002). Beard and Ochs (1993) state that the initiation of warm rain is critically dependent on the presence of large cloud droplets of which they found is most directly affected by the CCN distribution. Further, several studies found the nucleation of cloud drops on GCCN may cause the early formation of large cloud drops, which enhance the growth rate of cloud drops (Feingold et al. 1999; Blyth et al. 2003; Dagan et al. 2015). Some studies suggest high levels of aerosols in a cloud, which would lead to large droplet concentrations, are likely

associated with drizzle suppression (e.g., Bretherton et al. 2004; Wood et al. 2015). However, other studies have found that aerosol concentration predominantly affects the timing of precipitation onset rather than the precipitation rate (Wang et al. 2010; Mechem et al. 2012).

Precipitation onset in bulk microphysical parameterizations is represented by the process called autoconversion, which is designed to represent initiation of precipitation-sized drops through the coalescence of smaller droplets (Kessler 1969; Khairoutdinov and Kogan 2000). In recent two-moment parameterizations, autoconversion is a function of both cloud-water mixing ratio and droplet concentration, for example $A \sim q_c^{2.47} N_c^{-1.79}$ in Khairoutdinov and Kogan (2000). This functional dependence suggests a stronger dependence on liquid water content (a thermodynamic or meteorological factor) than on droplet concentration (an aerosol factor). This functional form is consistent with recent studies that have also found that drizzle is more sensitive to the thermodynamic and meteorological factors of the cloud than to the aerosol perturbations (Wang et al. 2010; Mechem et al. 2012). Larger moisture content within a deeper cloud tends to initiate precipitation (Magaritz et al. 2009) as well as increase and sustain drizzle rates (Wang et al. 2010; Mechem et al. 2012). Furthermore, precipitation rate scalings tend to exhibit a similar emphasis on thermodynamic properties (e.g., h^3/N in van Zanten et al. 2005). Even if we accept the $A \sim q_c^{2.47} N_c^{-1.79}$ functional form to represent autoconversion, however, it is natural to ask whether the precipitation initiation process in any given cloud is driven by anomalously large values of cloud liquid water mixing ratio (q_c) or anomalously small values of cloud droplet concentration (N_c). This study explores the relative importance of these two factors on the precipitation initiation process.

Many studies have used large-eddy simulation (LES) models with size-resolving microphysics ('bin' microphysics) to explore the precipitation processes within stratocumulus clouds (e.g., Kogan et al. 1995; Stevens et al. 1998; Khairoutdinov and Kogan 1999; Ackerman et al. 2009). Whereas bulk microphysical parameterizations typically assume partial moments (typically a 'cloud' part and a 'precipitation' part) of the drop-size distribution (DSD), bin models at each grid point discretize the DSD into a finite number of size bins and then evolve the DSD by condensation and collision–coalescence (by solving the stochastic collection equation). Because bin models attempt to represent the continuous DSD instead of partitioning it into partial moments, they have no need of a separate autoconversion parameterization. Precipitation initiation is then characterized by the first appearance of water in the drizzle drop size range, typically taken to be greater than or equal to 25 μm. This threshold is somewhat arbitrarily used in the literature, but LES results suggest that on average a value of 25 μm corresponds to a threshold value below which droplets lose mass (i.e., are collected) and above which droplets gain mass (Khairoutdinov and Kogan 2000).

This paper utilizes bin-microphysics LES and backward parcel trajectory modeling to explore the dominant microphysical precursor conditions that lead to precipitation initiation in stratocumulus clouds. Trajectory analysis has a long history in investigations of microphysical processes (e.g. Stevens and Bretherton 1996; Feingold et al. 1998; Kogan 2006; Andrejczuk et al. 2008; Magaritz et al. 2009; Ovchinnikov et al. 2013), with some studies focusing on specific aspects of precipitation initiation related to liquid water content, turbulence, entrainment, and CCN concentration. In contrast to these previous trajectory studies, our approach first identifies regions of precipitation initiation and then

calculates backward trajectories from these regions to characterize the precursor conditions associated with precipitation initiation. Specifically, we aim to discover which factor predominately governs precipitation initiation, specifically, anomalously large q_c or anomalously small N_c, parameters chosen because of their functional influence on autoconversion. To accomplish this, we look at the behavior of q_c and N_c along back trajectories and statistically compare those trajectories to 'null' cases originating in drizzle-free regions. Chapter 2 discusses the LES model, our approach to identifying regions of precipitation onset, and the backward-trajectory calculations. Chapter 3 presents the results found from the LES and trajectory models, and Chapter 4 delves into a discussion and conclusions derived from our results.

Chapter 2

Methodology

2.1 LES Model Configuration

A large eddy simulation (LES) model with size-resolved (bin) microphysics is employed to give the best possible representation of marine boundary layer dynamics and warm-rain microphysical processes (Kogan et al. 1995). The LES model used in this analysis is the System for Atmospheric Modeling – Explicit Microphysics (SAMEX; Kogan et al. 2012; Mechem et al. 2012). The dynamical core is based on the System for Atmospheric Modeling (SAM; Khairoutdinov and Randall 2003) and employs the anelastic equations of motion and monotonic, positive-definite advection for scalar quantities (Smolarkiewicz and Grabowski 1990). Subgrid-scale fluxes in SAMEX are parameterized using a 1.5-order subgrid-scale parameterization of Deardorff (1980).

The explicit (bin) representation of microphysical processes in SAMEX is based on Kogan (1991) and includes size-resolving representations of liquid water and soluble CCN. The droplet spectrum in SAMEX is represented by a single-moment mass distribution function. Condensation and evaporation employ a semi-Lagrangian approach and the variational optimization method of Liu et al. (1997) to remap to the drop spectrum to the Eulerian bins. The stochastic collection equation is computed by the method of Berry and Reinhardt (1974). All simulations use the Hall (1980) collection kernel and assume a coalescence efficiency of unity.

Data for the simulation setup are obtained from the Aerosol Radiation Measurement (ARM) Mobile Facility (AMF) located on Graciosa Island, Azores (39° 5’ 28” N, 28° 1’ 45” W)

during the CAP-MBL (Clouds, Aerosol, and Precipitation in the Marine Boundary Layer; Rémillard et al. 2012; Wood et al. 2015) field campaign that occurred May 2009 through December 2010. The goal of the CAP-MBL field campaign was to study the aerosol, cloud, and large-scale environmental conditions in the marine boundary layer (MBL).

The simulation is based on a case of persistent, single-layer, drizzling stratocumulus deck sampled through the majority of the day on 22 November 2009, as evident from the W-band ARM cloud radar (WACR) reflectivity field (Fig. 1). This case was chosen from the twenty-seven days during CAP-MBL where solid marine stratocumulus conditions prevailed (Luke and Kollias 2013). The case was also an ideal because the large-scale environment was predominantly barotropic, with zonal flow and little vertical wind shear.

Initial conditions for the LES model (potential temperature, mixing ratio, and *u* and *v* wind components) are based on the 1100 UTC 22 November 2009 sounding observation from Graciosa Island (Fig. 2), which shows a deep, well-mixed cloudy boundary layer. We assume a large-scale divergence of 3×10^{-6} s^{-1}, which corresponds to subsidence that increases from zero at the surface to 0.48 cm s^{-1} at the top of the boundary layer and above. Surface fluxes are calculated interactively using a fixed sea surface temperature (SST) of 290.4 K. CCN are assumed to be pure ammonium bisulfate, and two lognormal modes specify the total number of aerosols in each bin N = (65, 162.5) mg^{-1}, the width of the distribution σ_g = (1.1, 1.4) μm, and the center of the distribution r_g = (0.02, 0.05) μm, all constant with height. The CCN are 'diagnostic' in that they are not consumed by coalescence processing. Simulations are configured on a 96×96×150 grid with a horizontal grid spacing of 35 m. The vertical grid is stretched, with grid spacing of 5 m near the surface and inversion, and larger values in between and above. The model employs 19 CCN

bins and 25 mass-doubling cloud droplet bins. From the droplet spectra we calculate moment-based quantities such as liquid water content, mean radius, and radar reflectivity factor. Included in these calculations are separate liquid water mixing ratios, droplet concentrations, and mean volume radii for both the cloud and rain modes, defined using a threshold radius of 25 μm. The LES model is run for 9 total hours with collision-coalescence turned off for the first hour to spin up boundary layer turbulent flow.

2.2 Parcel Trajectory Model and Precipitation Initiation

We calculate backward trajectories using the method of Doty and Perky (1993) and Mechem et al. (2002) to analyze the precursor conditions of precipitation initiation in marine stratocumulus. Details about the trajectory calculation are presented in Appendix A. For each nascent precipitation cell identified, 1,000 trajectories are calculated from the LES output data. The nascent precipitation regions are quite small at this stage. Consequently, the volume of the trajectory initialization regions are equally as small, generally ~100–200 m in both horizontal and vertical directions. Because the nascent precipitation drops are small at the initiation stage, we are neglecting terminal fall speed of droplets in the trajectory calculation (something not justifiable once precipitation droplets grow to sufficient size to have an appreciable terminal fall speed).

We developed a method of identifying regions of nascent precipitation using a combined analysis of precipitation mixing ratio (q_r) and LWP of precipitation-sized droplets (droplet radius ≥ 0.25 μm; LWP_p). Multiple unsuccessful methods were attempted before we developed this final approach, including using a simulated reflectivity threshold, a liquid water content threshold, and a single precipitation mixing ratio threshold. For our

final method, robust cells of drizzle are first identified in contour plots of LWP_p and column-maximum q_r (Fig. 3). We determined that the ranges of 5.0 g $m^{-2} \geq LWP_p \geq$ 15.0 g m^{-2} and 0.01 g $kg^{-1} \leq q_r \leq$ 0.055 g kg^{-1} are optimal for identifying nascent drizzle cells. We acknowledge that these optimal ranges may not be universally applicable and may be somewhat case-dependent. Therefore, the identified robust drizzle cells are followed backward through time until $LWP_p \geq$ 5.0 g m^{-2} contour (Fig. 3) first appears for the cell. From here, we analyze the column-maximum q_r plot as well as vertical cross sections of q_r in both horizontal directions (Fig. 3) at the time and location of the LWP_p contour. The cell must lie in the contour where 0.01 g $kg^{-1} \leq q_r \leq$ 0.055 g kg^{-1} in all plots. If this condition is true, then this time and location is considered to be a region of precipitation initiation where the parcel trajectory model is initiated. These criteria identify the early stages of what will eventually become vigorous drizzle cells. The cells are captured early enough in their life cycle that they have not experienced appreciable collection or coalescence processing.

We compute 1,000 20-minute backward trajectories for ten nascent drizzle cells ('P', precipitating cases) we have identified. We explore the behavior of the bulk microphysical moments along the back trajectories, concentrating particularly on N_c, q_c, and mean volume radius r_v. In order to compare to a non-precipitating baseline, we also calculate backward trajectories for ten areas of the cloud where drizzle is not present ('N', null cases). Statistics from backward trajectories from our precipitating cases are compared with those from the nonprecipitating N cases.

We performed tests for all the P cases to evaluate the sensitivity of the back trajectories to choice of trajectory start time by varying the initial trajectory time by ±2-5

minutes of the control trajectory calculation. Comparing the output of these sensitivity experiments to the output of the original cases results in no significant difference in the analysis, suggesting a robustness of each case to our choice of precipitation initiation region.

Chapter 3

Results

3.1 Mean Cloud Behavior

The analysis period from 2 to 9 hours is characterized by a consistently homogeneous cloud that forms regions of long-lasting drizzle. Fig. 4 gives a snapshot of maximum column simulated reflectivity (Z) at 5 hr. Two of these strong, mature drizzle cells are highlighted with vertical cross sections of Z, q_r, q_c, and N_c. The reflectivity signature in the drizzle cells throughout the simulation remain smaller than 0 dBz. Both cross sections show that, even in the cells with the strongest reflectivity, drizzle dissipates ~0.8 km above the ground and does not reach the surface. These reflectivity signatures roughly resemble the observational WACR image in Fig. 1 (the 3-km sections in Fig. 4 would correspond to a time interval of ~10 minutes in from the profiling radar, assuming an advective speed of 5 m s^{-1}). The overlayed vertical velocity contours depict that these cells are dominated by weak updrafts and downdrafts predominantly smaller than 1 m s^{-1} in magnitude. Larger magnitudes of q_r (0.055 g kg^{-1} < q_r < 0.1 g kg^{-1}) accompany the strongest location of these cells, as do depressed concentrations of N_c (N_c < 70 cm^{-3}). Contours of q_c are fairly homogeneous throughout the domain. That is, in-cloud variability of q_c is less than variability of q_r.

The boundary layer is consistently deep (~1.6 km) over the whole simulation (Fig. 5), and cloud fraction remains near 100% (not shown), typical of a persistent deck of stratocumulus. LWP steadily increases somewhat throughout the simulation, ranging from ~80 g m^{-2} to ~120 g m^{-2}, whereas N_c remains nearly constant after model spin-up.

Mean profiles, averaged from 4–6 hours in the simulation, show that the boundary layer is well mixed with no discernable difference in liquid water potential temperature θ_l from the surface to the inversion base (Fig. 6a). The total water profile q_t (Fig. 6b) is well mixed to the inversion base except near the surface where an abrupt moisture decrease about 3.0 g kg^{-1} occurs. The liquid water profile q_l (cloud water plus precipitation; Fig. 6c) peaks sharply by about 0.45 g kg^{-1} in the upper part of the cloud (~1.6 km). This profile is dominated by the cloud-water category (q_c). These thermodynamic profiles closely represent profiles of an ideal stratocumulus case.

The vertical velocity variance $\overline{w'w'}$ profile (Fig. 7a) displays a single peak near 0.8 km in the boundary layer, further suggesting that the boundary layer is well mixed. The weak local maximum near the inversion (~1.3 km) is possibly a symptom of excess entrainment, which from our experience may arise from the model numerics. The vertical velocity skewness profile in Fig. 7b is weakly negative up to the inversion, suggesting the boundary layer is slightly dominated by stronger, narrower downdrafts driven by cloud-top radiative cooling. The positive spike in skewness near cloud top is commonly seen in stratocumulus (Moeng and Rotunno 1990; Stevens et al. 2003; Stevens et al. 2005) and has historically been interpreted as arising from a small number of surface-based updrafts and weaker downdrafts covering a broad area.

Background drizzle is persistent more-or-less throughout the entire simulation (i.e., drizzle water contents of $q_r > 0.01$ g kg^{-1}). It is important to note that this background drizzle does not represent precipitation initiation regions. Rather, we are searching for regions where this light background drizzle becomes strong, robust drizzle cells. The prevalence of background drizzle may be a model artifact caused by overly dispersive DSDs

in the Eulerian bin-model framework (Liu et al. 1997). However, the observational WACR image in Fig. 1 shows that drizzle is indeed present most of the day on 22 November 2009.

3.2 Trajectory Behavior

The contours in Fig. 8 are cross sections from the LES results representing the conditions of Z, q_r, q_c, and N_c for the center location of the trajectory volume in the nascent drizzle cell. From this time, the trajectories are integrated backward in time. To minimize confusion, we consistently describe trajectory movement through time in a typical, forward-in-time fashion.

The backward trajectories from regions of precipitation initiation exhibit three distinct characteristic behaviors. The first characteristic (CB, cloud base) has the majority of trajectories moving from below or near cloud base and into the cloud as they become the sampled cell (four cases). With the second characteristic (CT, cloud top), the majority of trajectories begin higher in the cloud and fall lower in the cloud before moving horizontally as they become the sampled cell (two cases). The third characteristic (CA, all cloud) is a combination of CB and CT (four cases). Fig. 8 shows examples of CB, CT, and CA trajectory behaviors.

As mentioned before and evident in Fig. 8, all cases are initialized in regions of the contour $0.01 \leq q_r \leq 0.055$ g kg^{-1}, though most trajectories end in regions where $q_r \leq 0.025$ g kg^{-1} (not shown). Fig. 8 depicts the majority of trajectories ending in regions with lower reflectivities and N_c values, specifically where $Z < 0.0$ dBz and $N_c < 60.0$ cm^{-3}. In some cases, the trajectories are initialized near regions of high N_c concentrations, as seen in Case 3 (Fig.

8). Also, considering the homogeneous nature of q_c, most trajectories end in regions where 0.1 g kg^{-1} ≤ q_c ≤ 0.5 g kg^{-1}.

Fig. 8 demonstrates the distinct behavior of the trajectory ensembles for the three example cases. Most CB cases begin with all trajectories lying in the subcloud layer, and in the example CB case 75% of the trajectories reach the cloud within 10-15 minutes (Fig. 9a). By 17 minutes, all trajectories are inside the cloud. The mean volume radius of droplets in the cloud spectrum r_v is included in our analysis because of the importance of large droplets to precipitation initiation. The variables r_v, q_r, and q_c are not conservative thermodynamic variables, and as such we do not expect them to remain constant along a trajectory. The behavior of average trajectory r_v for the example CB case (Fig. 10) increases through time as the trajectories rise in the cloud and capture the production of embryonic drizzle droplets. The trajectories' in-cloud (q_c > 0.01 g kg^{-1}) q_c values are consistent with vertical ascent through increasing adiabatic liquid water content values. The behavior of the trajectory N_c values in the cloud spectrum for the CB case is somewhat noisy early in the trajectory calculation because of the small number of trajectories in the cloud. As more trajectories enter into the cloud, average trajectory N_c remains fairly constant or increases slightly, staying mostly in the range of 40 cm^{-3} ≤ N_c ≤ 60 cm^{-3}. This behavior is expected as N_c should be well conserved in droplets that reside inside the cloud and away from supersaturated regions of droplet nucleation.

In the CT cases, the majority of trajectories remain in the upper part of the cloud throughout the trajectory calculation (e.g. Fig. 9b). The average trajectory r_v in the example CT case decreases as the trajectories move downward in the cloud and then increases as they rise again, finally resulting in the formation of drizzle embryos. Not all CT cases exhibit

this behavior, however. Average trajectory q_c values for the example CT case (e.g. Fig. 11) begin larger than the CB cases since these trajectories initiate high in-cloud. The q_c values then slightly decrease as some trajectories fall in the cloud and then increase again as trajectories rise in the cloud, ultimately forming the nascent precipitation cell. The average trajectory N_c is relatively stable in the CT cases where the trajectories spend most of their time in the cloud, as the CT example case demonstrates. This is consistent with the notion that droplet activation regions in stratocumulus, and hence local perturbations in N_c, lie close to cloud base. Some variability in N_c near cloud top may be attributable to the well-known behavior of spurious supersaturation at cloud top exhibited by Eulerian models (Stevens et al. 1996). In the other CT case (not shown), the average trajectory N_c decreases as the trajectories move fairly quickly to near cloud base and ~50% of trajectories move below cloud base. This decrease is attributed to mixing of cloudy and clean air parcels near cloud base. The N_c concentrations increase as the parcels are pulled back into the cloud and stabilizes as mixing ceases.

With the CA cases, the number of trajectories residing in-cloud behaves similar to the CB cases (i.e., similar to the example case in Fig. 9c). The behavior of the CA average trajectory r_v values depends the proportion of CB and CT trajectories, which varies by case. The cases where more trajectories begin near or just below cloud base behave more like the CB average trajectory r_v, such as the case shown in Fig. 12. CA cases where more trajectories begin near cloud top behave more like CT cases. The same is true for average trajectory values of q_c. Like the other two categories, the CA average trajectory N_c concentration remains mostly constant, as evident in the example case. For this reason, the CA category can be viewed as an intermediate category between the CB and CT categories.

In contrast to the precipitating trajectories, all of the non-precipitating 'N' trajectory cases behave similarly. The majority of trajectories begin below cloud base and rise into the cloud (not shown). The average trajectory r_v of the N cases does increase slightly over time as more trajectories flow into the cloud and rise toward higher levels. This is evident in the average trajectory q_c values increasing with time, as do the P cases. Somewhat counterintuitively, most N cases begin with higher values of q_c (≥ 0.2 g kg^{-1}) than the P cases and increase to larger final values as well ($q_c \approx 0.5$ g kg^{-1}). The average droplet concentration N_c along trajectories in the N cases is relatively constant over time, although they are at much larger concentrations than droplet concentrations in the P cases. This distinction between P and N cases will prove ultimately important in explaining drizzle initiation in the simulations.

3.3 Statistical behavior of the trajectories

Fig. 13 compares mean PDFs of r_v, q_r, q_c, and N_c composited from the last minute of all the P and N trajectory calculations, which we take in the P regions as being representative of the region of precipitation initiation. The PDFs are calculated only for when the trajectories reside in the cloud ($q_c \geq 0.01$ g kg^{-1}) since we are only interested in the cloud characteristics affecting precipitation initiation. For the P cases, this figure reinforces the results presented above. The trajectories in the nascent precipitating regions have larger r_v and q_r values than the N cases, a finding consistent with the distinction between parcels that eventually form drizzle-size drops and parcels that remain nonprecipitating cloud. Furthermore, compared to the N cases, the P trajectories have lower values of q_c and substantially lower values of N_c.

Fig. 14 compares mean PDFs of r_v, q_r, q_c, and N_c composited from the entire 20-minute trajectory calculation for both the P and N cases. As for Fig. 13, these PDFs are also calculated only for when the trajectories reside in the cloud ($q_c \geq 0.01$ g kg^{-1}). In contrast to the PDFs in Fig. 13, these 20-minute PDFs can in some sense be interpreted as a time-integral of the properties along the trajectories for the entire 20-minute trajectory calculation. This is the main reason why the PDFs in Fig. 14 are broader than those shown in Fig. 13 as they are representing the conditions the droplets experience from the beginning of the trajectory calculation up through the time of the nascent drizzle cell depicted in Fig. 13. We compare the P and N PDFs of each variable not only to ensure that the P cases we use are dissimilar to the N cases and consequently not initialized too early but also to determine whether N_c or q_c more strongly governs precipitation initiation. The r_v distributions for both P and N categories appear similar. However, the secondary peak in the P distribution around 12 μm along with the longer tail ($r_v > 14$ μm) signifies the parcels in the P cases contain larger droplets that will eventually become nascent drizzle, whereas the majority of parcels in the N cases stop growing after they reach ~10 μm.

It is also clear that the P and N PDF distributions for q_r, q_c, and N_c differ greatly. As to be expected, the N q_r PDF peaks very close to 0.0 g kg^{-1}, much lower than the P PDF, as these are non-precipitating cases. The tail of larger N values is associated with the few outlier trajectories that may briefly move through small cells of higher q_r values. P N_c peaks at 50 cm^{-3}, much lower than the N's peak around 110 cm^{-3}. P q_c also peaks much lower than the N, with a peak near 0.1 g kg^{-1} compared to a peak of ~0.45 g kg^{-1}. These are surprising results that do not match our initial hypothesis that precipitation initiation would be driven largely by larger values of liquid water content.

Table 1 reports the first, second, and third moments from the P and N PDFs. Comparing the first moments of the P and N PDFs, we see that they match with the previous analysis of the PDF peaks: P N_c and q_c are both smaller than the N, P q_r is larger than the N, and P and N r_v are similar. This result holds true with each PDF's standard deviation, as well.

Skewness results report that none of the distributions are normal. However, the P r_v, q_r, and N_c PDFs and the N q_c PDF are all closer to a normal distribution than their counterparts which suggests that the trajectories in those runs have a more evenly distributed spread. Taking a closer look at each variable in turn, the negative, more heavily skewed N r_v indicates that the N cases have tails with much smaller values than the P cases, again indicating nascent drizzle in the P cases. The larger positive skewness for P q_c indicates there is a larger tail to the right compared to the left tail on N q_c's PDF. The P N_c PDF is only very slightly positively skewed which implies that it only has slightly more values greater than its mean and, more importantly, that most of the N_c values are relatively small (since the mean is small). The N N_c PDF is strongly negatively skewed where the majority of the values are much larger than the P N_c PDF values.

We calculate multiple statistical measures to determine whether differences between the P and N distributions are statistically significant. We use the Welch's t-test assuming unequal variances to test the significance of the differences in the means of the P and N PDFs, and the F-test to determine the significance of the differences in variance of the P and N PDFs (Table 2). The q_r, q_c, and N_c means are statistically significant at the $\alpha = 0.05$ significance level. Differences in N_c and q_r variances are significant as well. To more completely evaluate differences in the PDFs, we also apply the Kolvogorov-Smirnoff test

(Appendix B) to the cumulative density functions (Fig. 15) of the P and N trajectory PDFs. This test reports that the differences in the r_v and q_c CDF's are also statistically significant at the $\alpha = 0.05$ significance level.

Chapter 4

Summary and Conclusions

In this study, we calculate backward trajectories from LES model output to explore microphysical precursor conditions behind precipitation initiation for a specific case of drizzling marine stratocumulus cloud sampled during the CAP–MBL field campaign. We employ the bin microphysical model SAMEX initialized with the 1100 UTC 22 November 2009 sounding observations from Graciosa Island. This is an ideal case as it displays a persistent, single-layer, drizzling stratocumulus deck and a predominantly barotropic environment. We calculate from the droplet spectra moment-based quantities including separate liquid water mixing ratios, droplet concentrations, and mean volume radii for both the cloud and rain modes.

From the LES output data we calculate 20-minute backward trajectories initiating from regions of nascent precipitation that are identified through analysis of drizzle-water mixing ratio (q_r) and LWP of precipitation-sized drops (LWP_p). We analyze the properties of bulk microphysical quantities like N_c, q_c, q_r, and r_v along the parcel trajectories of ten cases of nascent precipitation and ten non-precipitating cases to determine the microphysical conditions the parcels experienced as they move through space and time. In bulk microphysical parameterizations, drizzle initiation is represented by the autoconversion process, which for one parameterization has the form $A \sim q_c^{2.47} N_c^{-1.79}$. We characterize the bulk, moment-based quantities along the back trajectories to evaluate whether nascent drizzle cells are associated with regions of anomalously large q_c or anomalously small N_c.

Back-trajectory paths for each precipitating case fall into three distinct characteristic behaviors: CB where the majority of trajectories begin near or below cloud base, CT where the majority of trajectories begin higher in the cloud, and CA where the trajectories are split between the CB and CT. The average behaviors of the examined microphysical properties generally coincide with the movement of the trajectories through the cloud. As trajectories and the accompanying cloudy parcels in the CB and CA cases rise over time, the average q_c concentrations and r_v values of the parcels slowly increase, a simple result of increasing adiabatic liquid water content with height. In the last 5-10 minutes of each P trajectory calculation, r_v values increase significantly as nascent drizzle drops form.

Average PDFs of all of the microphysical variables over the 20-minute trajectory calculations indicate that the P and N cases are largely distinct, and a number of statistical tests are employed to evaluate whether the P and N PDFs of different variables are significantly different. From the trajectory PDFs, we find that the trajectory-mean q_c value in these P cases is actually smaller than the in the N cases, which runs counter to our working hypothesis that parcels eventually forming drizzle would be the ones experiencing large values of liquid water along their trajectories. The average N_c concentrations of the parcels in all three P behaviors remain fairly constant when the majority of trajectories are cloud-sized droplets, but the mean N_c values in the P case were smaller than in the N case. *These results indicate the most surprising aspect of our study, specifically that the larger values of mean volume radius (r_v) in the P cases are driven, not by large cloud liquid water contents (q_c), but rather by small values of cloud droplet concentration (N_c).* This result seems to run counter to the findings of Wang et al. (2010) and Mechem et al. (2012), who

both emphasize the influence of thermodynamics (e.g., deeper or moisture boundary layers leading to larger liquid water content values) on drizzle production. One passible route to resolve the discrepancy between the findings is to note that this study investigates the conditions associated with small-scale drizzle initiation, whereas those two studies (in addition to the field-campaign precipitation scalings) address cloud-system behavior, which is an integral quantity obtained from the combined effects of many individual precipitation cells.

We conclude that the results from our trajectory analysis are not attributable to collection and CCN scavenging by each individual identified cell. Rather, they suggest that these new regions of nascent drizzle form from parcels that have previously experienced scavenging and collection and therefore as part of previous drizzle production. We acknowledge that this finding may be a product of aggressive coalescence processing due to our model configuration.

The relatively consistent drizzle throughout time and space in our case made it trickier than expected to find brand new, embryonic drizzle cells. Here we suggest alternatives that could make it easier to attempt to catch brand new cells and not regions that are products of previously precipitating cells. One suggestion is to identify cases at the very first time drizzle occurs in a model run to initialize trajectories from. Previous studies utilizing forward trajectory models have utilized this method (e.g. Magaritz et al. 2009; Feingold et al. 2013; Lee et al. 2014; Magaritz-Ronen et al. 2016). However, this could be difficult to perform with a backward trajectory model due to the spin-up time required in cloud models to initiate turbulence in the cloud. Another approach to this problem would be to utilize a backward trajectory analysis using model results of a shallow cumulus case.

It would be interesting to see how the results would differ with a case that forms more robust and isolated cells of precipitation than stratocumulus cases.

The backward trajectory analysis method of this study can be used to extend the analyses of precipitation onset performed in other studies. Recent methods have utilized the skewness field of the Doppler spectrum from profiling millimeter-wave cloud radar observations to identify regions of precipitation onset (e.g. Luke and Kollias 2013). This 'skewness' approach identifies regions of precipitation onset via the signal of small drizzle drops in the radar sampling volume. Unfortunately, the approach cannot step backward in time to examine the formation of these nascent drizzle regions. Our approach identifies these regions of precipitation initiation and then the associated precursor conditions as part of the turbulent, three-dimensional flow. This work was cast in terms of bulk microphysical factors, at least in part because of the influence of these factors in most current formulations of autoconversion. However, the next logical step is to perform a similar analysis of the same 22 November 2009 case exploring the evolution of the entire drop-size distribution along trajectories, or following simulated Doppler spectra obtained from forward radar model calculations of the model output fields. The Doppler spectra analysis in particular would conveniently compare with the Doppler cloud radar observations.

Appendix

Appendix A

Trajectory Calculation Methodology

The core calculations employed in the trajectory model are based on a combination of the Doty and Perky (1993) and Mechem et al. (2002) methods, which is equivalent to the baseline method utilized in HYSPLIT (Hybrid Single-Particle Lagrangian Integrated Trajectory model; Draxler and Hess 1998; Stein et al. 2015). The calculation is completed in two stages, denoted by subscripts 1 or 2. The superscript *i* represents the time step number, and Δt is the time integration time step, which is 1 second in this study.

The first stage estimates the new position of the parcels at timestep i+1

$$x_1^{i+1} = x_1^i + u_1 \Delta t$$

$$y_1^{i+1} = y_1^i + v_1 \Delta t$$

$$z_1^{i+1} = z_1^i + w_1 \Delta t$$

where the initial velocities are defined as

$$u_1 = u_1(x_1^i , y_1^i , z_1^i)$$

$$v_1 = v_1(x_1^i , y_1^i , z_1^i)$$

$$w_1 = w_1(x_1^i , y_1^i , z_1^i)$$

Stage 2 estimates the parcel velocities at the estimated new parcel positions calculated in Stage 1:

$$u_2 = u_2(x_1^{i+1} , y_1^{i+1} , z_1^{i+1})$$

$$v_2 = v_2(x_1^{i+1}, y_1^{i+1}, z_1^{i+1})$$

$$w_2 = w_2(x_1^{i+1}, y_1^{i+1}, z_1^{i+1})$$

The old and the new velocity components are then averaged:

$$\langle u \rangle = \frac{u_1 + u_2}{2}$$

$$\langle v \rangle = \frac{v_1 + v_2}{2}$$

$$\langle w \rangle = \frac{w_1 + w_2}{2}$$

These velocity averages are then used to calculate the final position:

$$x_2^{i+1} = x_1^i + \langle u \rangle \Delta t$$

$$y_2^{i+1} = y_1^i + \langle v \rangle \Delta t$$

$$z_2^{i+1} = z_1^i + \langle w \rangle \Delta t$$

Appendix B

Kolmogorov-Smirnoff Test

We utilize the Kolmogorov-Smirnoff test calculations described in Press et al. (1992). The Kolmogorov-Smirnoff (K-S) test is applied to compare the cumulative distribution functions (CDF) of two sets of data. The Kolmogorov-Smirnoff statistic D is defined as the maximum value of the absolute difference between two CDFs, $S_{N1}(x)$ and $S_{N2}(x)$:

$$D = \max_{-\infty<x<\infty} |S_{N1}(x) - S_{N2}(x)|$$

Determining the significance level of D involves the monotonic function

$$Q_{KS}(\lambda) = 2\sum_{j=1}^{\infty}(-1)^{j-1}e^{-2j^2\lambda^2}$$

This function has the limiting values

$$Q_{KS}(0) = 1 \qquad Q_{KS}(\infty) = 0$$

In terms of this function, the significance level of a value of D is given approximately by

$$\text{Probability } (D > \text{observed}) = Q_{KS}\left(\left[\sqrt{N_e} + 0.12 + 0.11/\sqrt{N_e}\right]D\right)$$

N_e is the effective number of data points

$$N_e = \frac{N_1 N_2}{N_1 + N_2}$$

Where N_1 is the number of data points in the first distribution and N_2 in the second.

In our case, we applied the K-S test to the drizzle and non-drizzle CDFs of the microphysical variables r_v, q_r, q_c, and N_c. Fig. 15 depicts the CDFs for each variable.

References

Ackerman, A. S., O. B. Toon, and P. V. Hobbs, 1993: Dissipation of marine stratiform clouds and collapse of the marine boundary layer due to the depletion of cloud condensation nuclei by clouds. *Science*, **262**, 226–229.

Ackerman, A.S., O. B. Toon, and P. V. Hobbs, 1995: Numerical modeling of ship tracks produced by injections of cloud condensation nuclei into marine stratiform clouds. *J. Geophys. Res.*, **100** (D4), 7121-7133.

Ackerman, A. S., and Coauthors, 2009: Large-eddy simulations of a drizzling, stratocumulus-topped marine boundary layer. Mon. Wea. Rev., **137**, 1083–1110.

Ackerman, A.S., M.P. Kirkpatrick, D.E. Stevens, and O.B. Toon, 2004: The impact of humidity above stratiform clouds on indirect aerosol climate forcing. *Nature*, **432**, 1014-1017.

Andrejczuk, M., J.M. Reisner, B. Henson, M.K. Dubey, and C.A. Jeffery, 2008: The potential impacts of pollution on a nondrizzling stratus deck: Does aerosol number matter more than type? *J. Geophys. Res.*, **113**, D19204.

Albrecht, B. A., 1989: Aerosol, cloud microphysics, and fractional cloudiness. *Science,* **245**, 1227–1230.

Beard, K.V., and H.T. Ochs III, 1993: Warm-rain initiation: An overview of microphysical mechanisms. *J. Appl. Meteor.*, **32**, 608-625.

Berry, E. X., and R. L. Reinhardt, 1974: An analysis of cloud drop growth by collection: Part III. Accretion and self-collection. *J. Atmos. Sci.,* **31**, 2118–2126.

Blyth, A.M., S.G. Lasher-Trapp, W.A. Cooper, C.A. Knight, and J. Latham, 2003: The Role of Giant and Ultragiant Nuclei in the Formation of Early Radar Echoes in Warm Cumulus Clouds. *J. Atmos. Sci.*, **60**, 21, 2557-2572.

Bretherton, C. S., T. Uttal, C. W. Fairall, S. E. Yuter, R. A. Weller, D. Baumgardner, K. Comstock, and R. Wood, 2004: The EPIC 2001 stratocumulus study. *Bull. Amer. Meteor. Soc.*, **85**, 967-977.

Dagan, G., I. Koren, and O. Altaratz, 2015: Aerosol effects on the timing of warm rain processes. *Geophys. Res. Lett.*, **24**, 4590-4598.

Deardorff, J. W., 1980: Stratocumulus-capped mixed layers derived from a three-dimensional model. *Bound-Layer Meteor.,* **18**, 495– 527.

Doty K.G., and D.J. Perkey, 1993: Sensitivity of Trajectory Calculations to the Temporal Frequency of Wind Data. *Mon. Wea. Rev.*, **121**, 387-401.

Draxler, R.R., and G.D. Hess, 1998: An overview of the HYSPLIT_4 modeling system of trajectories, dispersion, and deopositon. *Aust. Meteor. Mag.*, **47**, 295-308.

Feingold, G. A. McComiskey, D. Rosenfeld, and A. Sorooshian, 2013: On the relationship between cloud contact time and precipitation susceptibility to aerosol. *J. Geophys. Res. Atmos.*, **118**, 1-11.

Feingold, G., S.M. Kreidenweis, and Y. Zhang, 1998: Stratocumulus processing of gases and cloud condensation nuclei. I. Trajectory ensemble model. *J. Geophys. Res.*, **103**, D16, 19,572-19,542.

Feingold, G., W.R. Cotton, S.M. Kreidenweis, and J.T. Davis, 1999: The Impact of Giant Cloud Condensation Nuclei on Drizzle Formation in Stratocumulus: Implications of Cloud Radiative Properties. *J. Atmos. Sci.*, **56**, 4100-4117.

Hahn, C. J., and S. G. Warren, 2007: A gridded climatology of clouds over land (1971–96) and ocean (1954–97) from surface observations worldwide. Numeric Data Package NDP-026E ORNL/CDIAC-153, CDIAC, Department of Energy, Oak Ridge, TN.

Hall, W. D., 1980: A detailed microphysical model within a two-dimensional dynamical framework: Model description and preliminary results. *J. Atmos. Sci.*, **37**, 2486-2507.

Jiang, H., G. Feingold, and W. R. Cotton, 2002: Simulations of aerosol-cloud-dynamical feedbacks resulting from entrainment of aerosol into the marine boundary layer during the Atlantic Stratocumulus Transition Experiment. *J. Geophys. Res.*, **107**, 4813, doi:10.1029/2001JD001502.

Kessler, E., 1969: *On the Distribution and Continuity of Water Sub- stance in Atmospheric Circulation. Meteor. Monogr.,* No. 32, Amer. Meteor. Soc., 84 pp.

Khairoutdinov, M. F., and Y. L. Kogan, 1999: A large eddy simulation model with explicit microphysics: Validation against aircraft observations of a stratocumulus-topped boundary layer. *J. Atmos. Sci.,* **56,** 2115–2131.

Khairoutdinov M.F. and D.A. Randall, 2003: Cloud Resolving Modeling of the ARM Summer 1997 IOP: Model Formulation, Results, Uncertainties, and Sensitivities. *J. Atmos. Sci.*, **60**, 607-625.

Khairoutdinov, M.F. and Y. Kogan, 2000: A New Cloud Physics Parameterization in a Large-Eddy Simulation Model of Marine Stratocumulus. *Mon. Wea. Rev.,* **128**, 229-243.

Klein, S. A., and D. L. Hartmann, 1993: The seasonal cycle of low strati- form clouds. J. Climate, **6**, 1588–1606.

Kogan, Y.L., 1991: The simulation of a convective cloud in a 3-D model with explicit microphysics. Part I: Model description and sensitivity experiments. *J. Atmos. Sci.*, **40**, 1160-1189.

Kogan, Y.L., M.P. Khairoutdinov, D.K. Lilly, Z.N. Kogan, and Q. Liu, 1995: Modeling of stratocumulus cloud layers in a large eddy simulation model with explicit microphysics. *J. Atmos. Sci.*, **52**, 16, 2923-2940.

Kogan, Y.L., 2006: Large-Eddy Simulation of Air Parcels in Stratocumulus Clouds: Time Scales and Spatial Variability. *J. Atmos. Sci.*, **63**, 952-967.

Kogan, Y. L., D. B. Mechem, and K. Choi, 2012: Effects of sea-salt aerosols on precipitation in simulations of shallow cumulus. *J. Atmos. Sci.*, **69**, 463–483.

Lee, J. Y. Noh, S. Raasch, T. Riechelmann, and L.-P. Wang, 2014: Investigation of droplet dynamics in a convective cloud using a Lagrangian cloud model. *Meteorol. Atmos. Phys.*, **124**, 1-21.

Liu, Q.-F., Y. L. Kogan, D. K. Lilly, and M. P. Khairoutdinov, 1997: Variational optimization method for calculation of cloud drop growth in an Eulerian drop-size framework. *J. Atmos. Sci.,* **54**, 2493–2504.

Luke, E.P. and P. Kollias, 2013: Separating Cloud and Drizzle Radar Moments during Precipitation Onset Using Doppler Spectra. *J. Atmos. Oceanic Technol.*, **30**, 1656-1671.

Magaritz, L. M. Pinsky, O. Krasnov, and A. Khain, 2009: Investigation of Droplet Size Distributions and Drizzle Formation Using a New Trajectory Ensembe Model. Part II: Lucky Parcels. *J. Atmos. Sci.*, **66**, 781-805.

Magaritz-Ronen, L., M. Pinsky, and A. Khain, 2016: Drizzle formation in stratocumulus clouds: effects of turbulent mixing. *Atmos. Chem. Phys.*, **16**, 1849-1862.

Mechem, D.B, R.A. Houze Jr., and S.S. Chen, 2002: Layer inflow into precipitating convection over the western tropical Pacific. *Q. J. R. Meteorol. Soc.*, **128**, 1997-2030.

Mechem, D.B., S.E. Yuter, and S.P. de Szoeke, 2012: Thermodynamic and Aerosol Controls in Southeast Pacific Stratocumulus. *J. Atmos. Sci.*, **69**, 1250-1266.

Moeng, C.-H., and R. Rotunno, 1990: Vertical-velocity skewness in the buoyancy-driven boundary layer. J. Atmos. Sci., **47**, 1149– 1162.

Ovchinnikov, M., R.C. Easter, and W.I. Gustafson Jr., 2013: Untangling dynamical and microphysical controls for the structure of stratocumulus. *Geophys. Rea. Let.*, **40**, 4432-4436.

Press, W.H., S.A. Teukolsky, W.T. Vetterling, and B.P. Flannery, 1992: Statistical Description of Data. *Numerical recipes in C (2nd ed.): the art of scientific computing.* Cambridge University Press, 609-655.

Remillard, J., P. Kollias, E. Luke, and R. Wood, 2012: Marine Boundary Layer Cloud Observations in the Azores. *J. of Clim.*, **25**, 7381-7398.

Remillard, J., P. Kollias, A. Fridlind, A. Ackerman, G. Tselioudis, D. Mechem, H. Chandler, E. Luke, P. Chuang, M. Witte, D. Rossiter, and R. Wood, 2016: Observational constraint of drizzle properties and processes in large-eddy simulations from two models with size-resolved microphysics. *ASR Science Team Meeting*, 2-6 May 2016, Tysons, VA.

Smolarkiewicz, P. K., and W. W. Grabowski, 1990: The multidimensional positive definite advection transport algorithm: Non-oscillatory option. J. Comput. Phys., **86**, 355–375.

Stein, A.F., R.R. Drazler, G.D. Rolph, B.J.B. Stunder, M.D. Cohen, and F. Ngan, 2015: NOAA'S HYSPLIT atmospheric transport and dispersion modeling system. *Bull. Amer. Meteor. Soc.*, **96**, 2059-2077, http://dx.doi.org/10.1175/BAMS-D-14-00110.1.

Stephens, G. L., and T. J. Greenwald, 1991: Observations of the Earth's radiation budget in relation to atmospheric hydrology. Part II: Cloud effects and cloud feedback. J. Geophys. Res., **96**, 15 325–15 340.

Stevens, D.E. and S. Bretherton, 1996: A forward-in-time advection scheme and adaptive multilevel flow solver for nearly incompressible atmospheric flow. *J. Comput. Phys.*, **129**, 284-295.

Stevens, B., R. L. Walko, W. R. Cotton, and G. Feingold, 1996: Spurious production of cloud-edge supersaturations by Eulerian models. *Mon. Wea. Rev.*, **124**, 1034-1041.

Stevens, B., W.R. Cotton, G. Feingold, and C.-H. Moeng, 1998: Large-eddy simulations of strongly precipitating, shallow, stratocumulus-topped boundary layers. *J. Atmos. Sci.*, **55**, 3616-3638.

Stevens B., and Coauthors, 2003: On entrainment rates in nocturnal marine stratocumulus. Quart. J. Roy. Meteor. Soc., **129**, 3469– 3493.

Stevens, B., and Coauthors, 2005: Evaluation of large-eddy simulations via observations of nocturnal marine stratocumulus. *Mon. Wea. Rev.*, **133**, 1443-1462.

vanZanten, M.C., B. Stevens, G. Vali, and D.H. Lenschow, 2005: Observations of drizzle in nocturnal marine stratocumulus. *J. Atmos. Sci.*, **62**, 88-106.

Wang, H., G. Feingold, R. Wood, and J. Kazil, 2010: Modelling microphysical and meteorological controls on precipitation and cloud cellular structures in southeast Pacific stratocumulus. *Atmos. Chem. Phys.*, **10**, 6347-6362.

Warren, S. G., C. J. Hahn, J. London, R. M. Chervi, and R. L. Jenne, 1986: Global distribution of total cloud cover and cloud type amounts over land. NCAR Tech. Note TN– 2731STR, 29 pp. 1 200 maps. [Available from the National Center for Atmospheric Research, Boulder, CO 80307–3000.]

Wood, R., M. Wyant, C.S. Bretherton, J. Remillard, P. Kollias, J. Fletcher, J. Stemmler, S. de Szoeke, S. Yuter, M. Miller, D. Mechem, G. Tselioudis, J.C. Chiu, J.A.L. Mann, E.J. O'Connor, R.J. Hogan, X. Dong, M. Miller, V. Ghate, A. Jefferson, Q. Min, P. Minnis, R. Palikonda, B. Albrecht, E. Luke, C. Hannay, and Y. Lin, **2015**: Clouds, Aerosol, and Precipitation in the Marine Boundary Layer: An ARM Mobile Facility Deployment. *Bull. Amer. Meteor. Soc.*, 96, 419-440.

Tables

Table 1. Statistical moments of P and N 20-minute averaged PDFs for r_v, q_r, q_c, and N_c.

	r_v (μm)		q_r (g kg^{-1})		q_c (g kg^{-1})		N_c (cm^{-3})	
	P	N	P	N	P	N	P	N
Mean	9.58	9.18	0.0073	0.0017	0.20	0.34	47.28	95.11
SD	1.89	1.69	0.0041	0.0019	0.13	0.17	14.05	23.59
Skewness	-0.23	-1.24	0.62	1.82	0.54	-0.20	0.0035	-0.77

Table 2. Welch's t-test, F statistic, and Kolmogorov-Smirnoff (K-S) statistic and their respective probability values for the P vs. N 20-minute averaged PDFs for r_v, q_r, q_c, and N_c. Asterisk represents statistically significant probability values at the 95% confidence level.

	t-test	p	F statistic	p	K-S statistic	p
r_v	1.22	0.22	1.25	0.40	0.11	0.79
q_r	7.05	0.78e-8*	4.40	0.66e-4*	0.36	0.012*
q_c	-4.32	0.47e-4*	1.79	0.070	0.22	0.24
N_c	-14.47	0.27e-26*	2.81	0.31e-5*	0.35	0.32e-3*

Figures

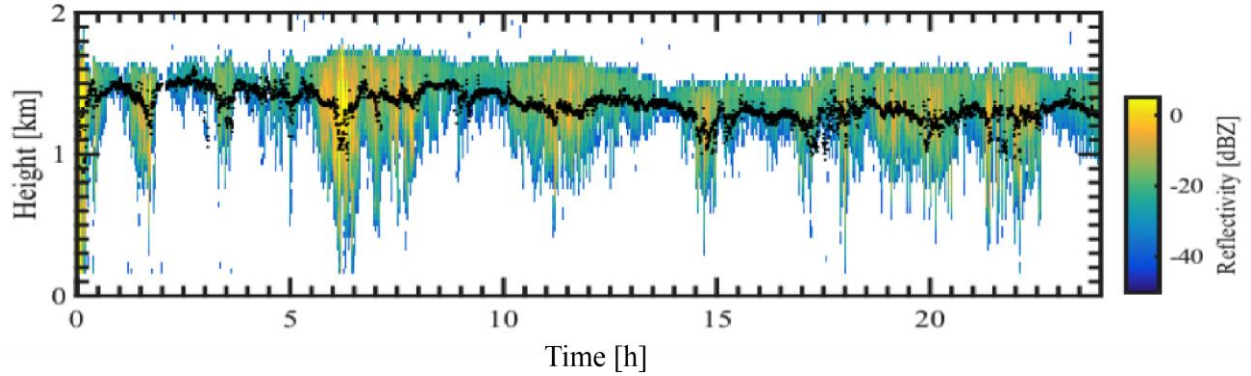

Fig. 1. Radar reflectivity factor observed during the whole day of 22 November 2009. Black dots represent the cloud-base height retrieved by the ceilometer. (Remillard et al. 2016)

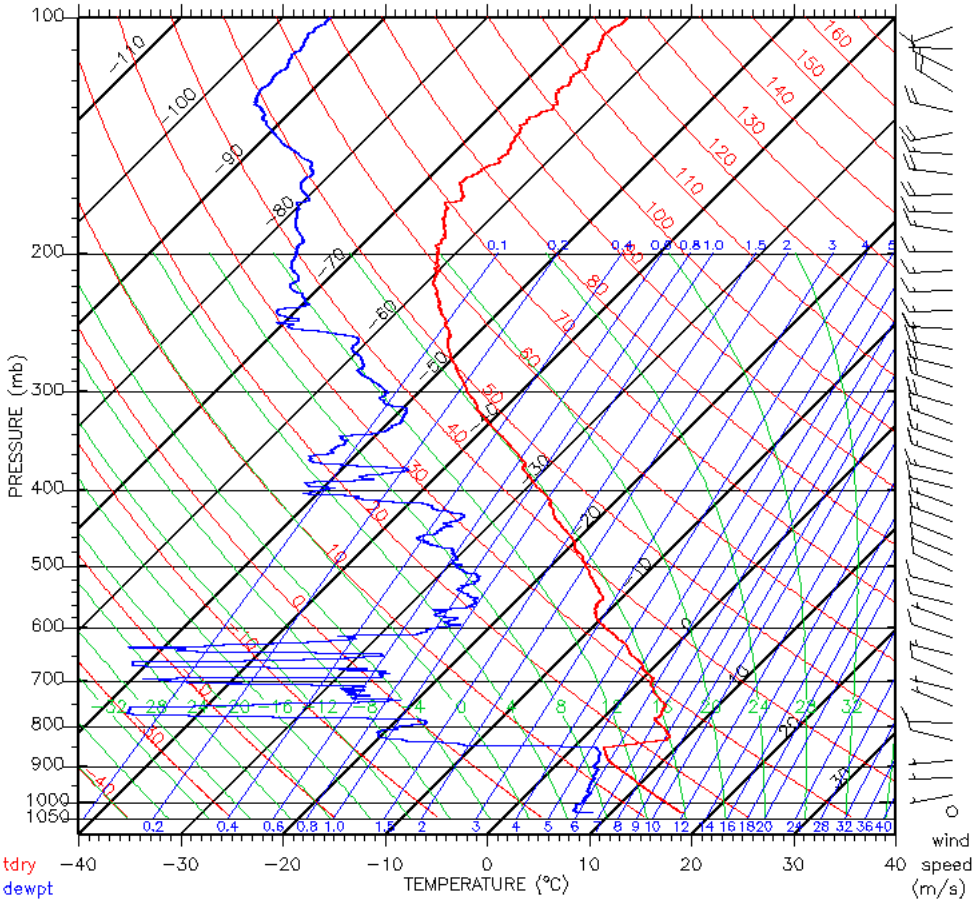

Fig. 2. The 11 UTC 22 November 2009 atmospheric sounding from which initial conditions for the LES run are based.

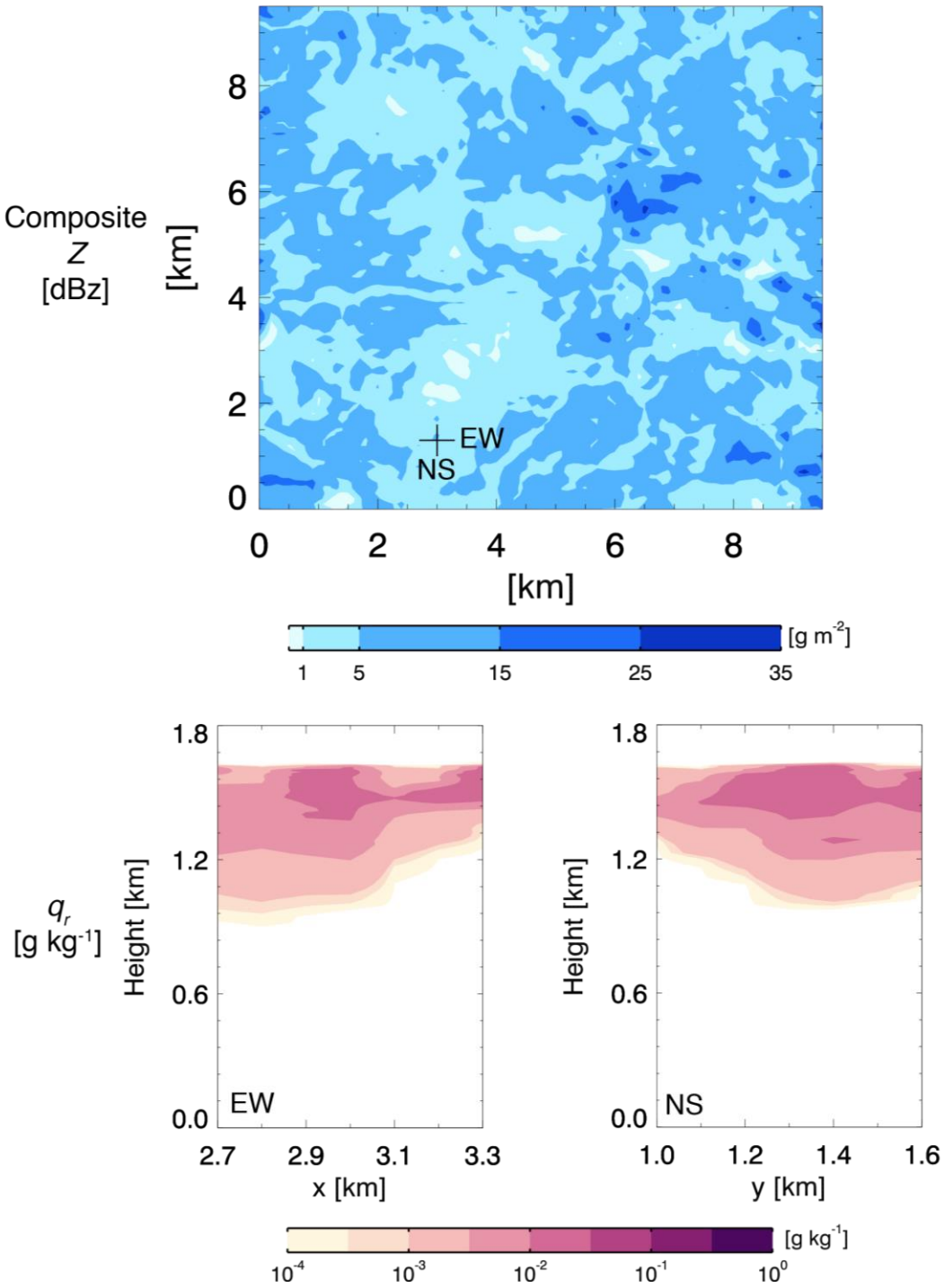

Fig. 3. Examples of model output figures used to identify regions of nascent precipitation. Top: Liquid water path of precipitation-sized droplets LWP_p. Bottom: Vertical cross sections of rain water mixing ratio q_r through the black lines in LWP_p figure. All figures are at 198 min.

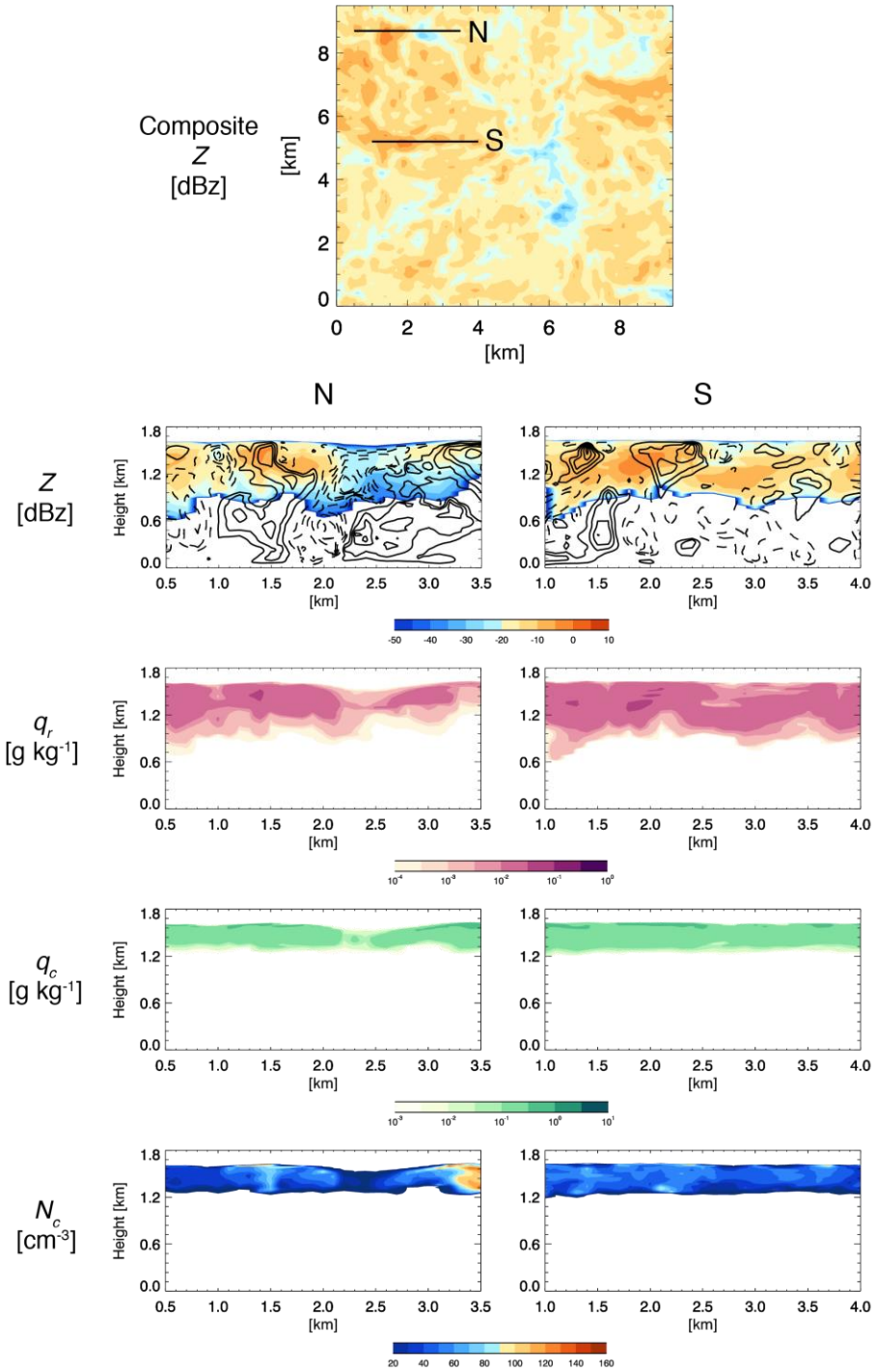

Fig. 4. Simulated composite reflectivity at 5 hour of the LES simulation and vertical cross sections of simulated reflectivity, q_r, q_c, and N_c through the black lines overlayed on the composite simulated reflectivity. The contours over the simulated reflectivity cross section represent vertical velocity values every 0.25 m s^{-2}, with dashed contours representing negative values.

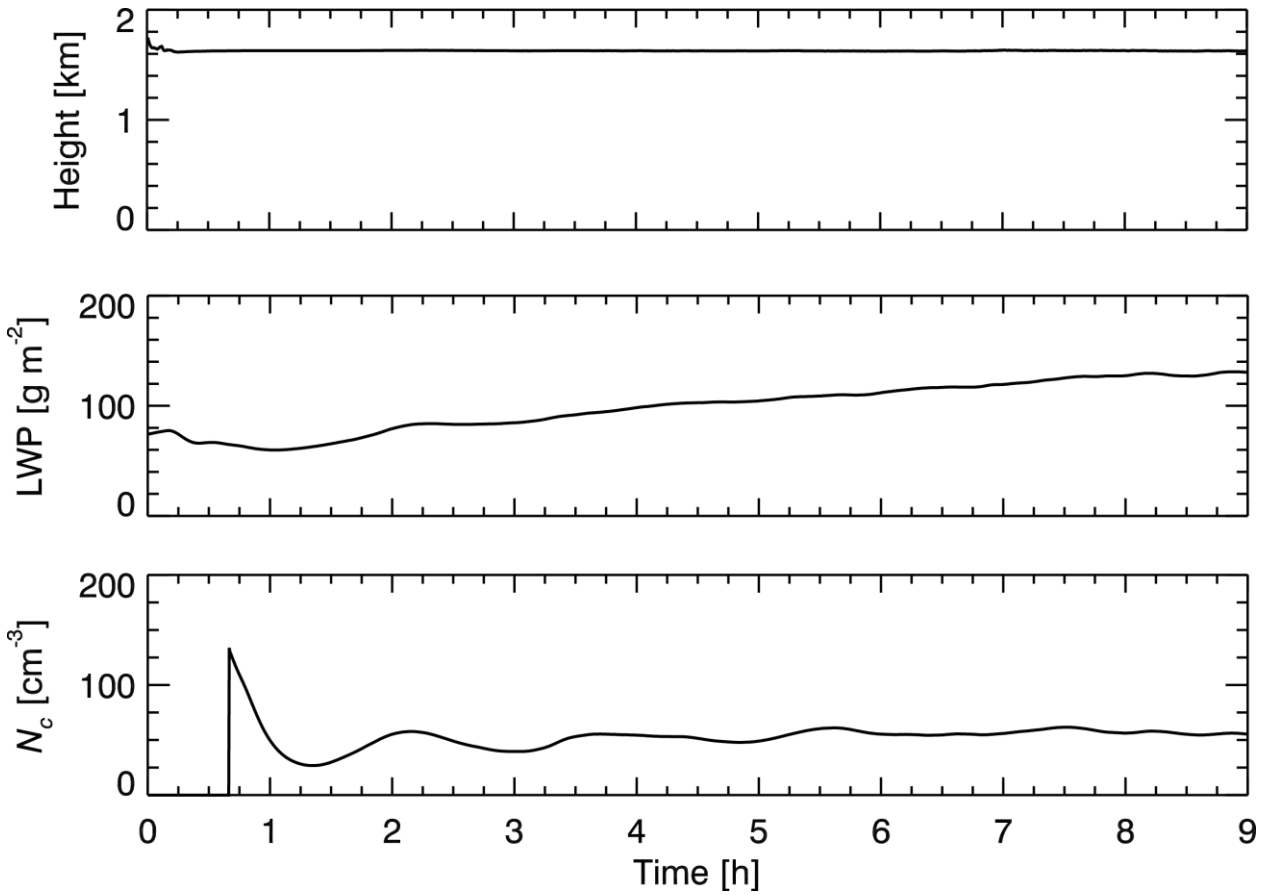

Fig. 5. Time series of boundary layer depth, liquid water path, and cloud droplet concentration representing mean cloud behavior of the LES simulation.

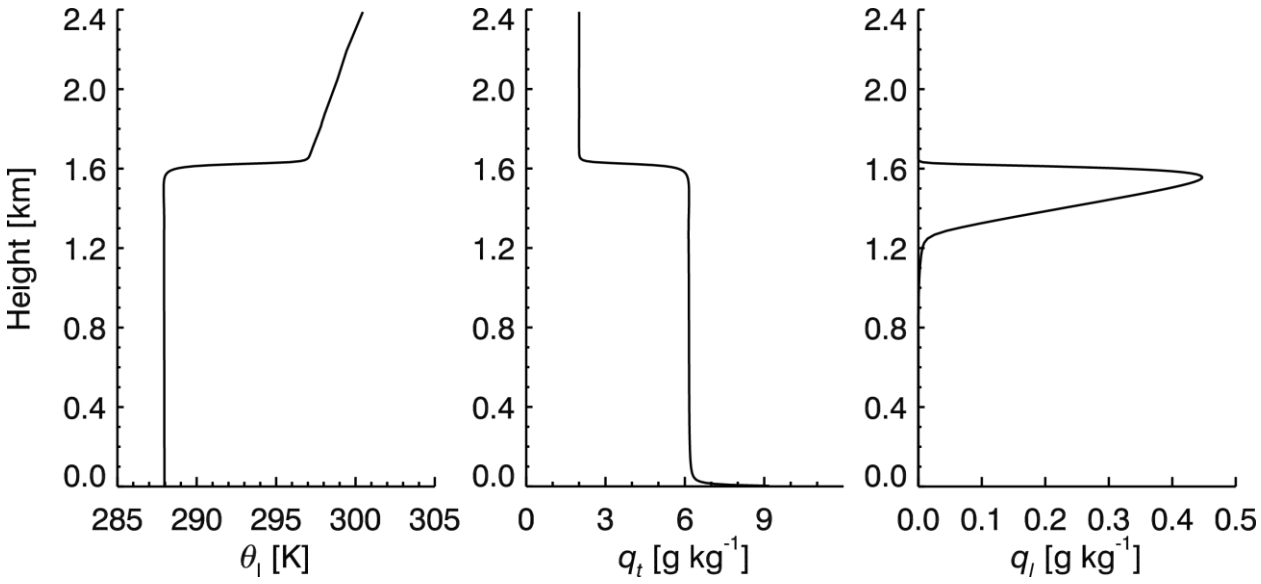

Fig. 6. Mean profiles for hours 4-6 of liquid water potential temperature θ_l, total water mixing ratio q_t, and liquid water mixing ratio ql.

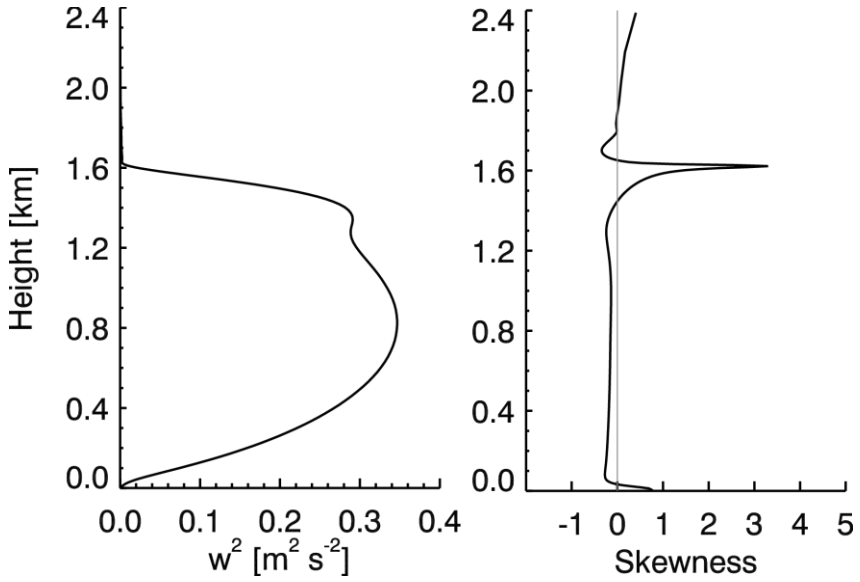

Fig. 7. Mean profiles for hours 4-6 of vertical velocity variance and vertical velocity skewness.

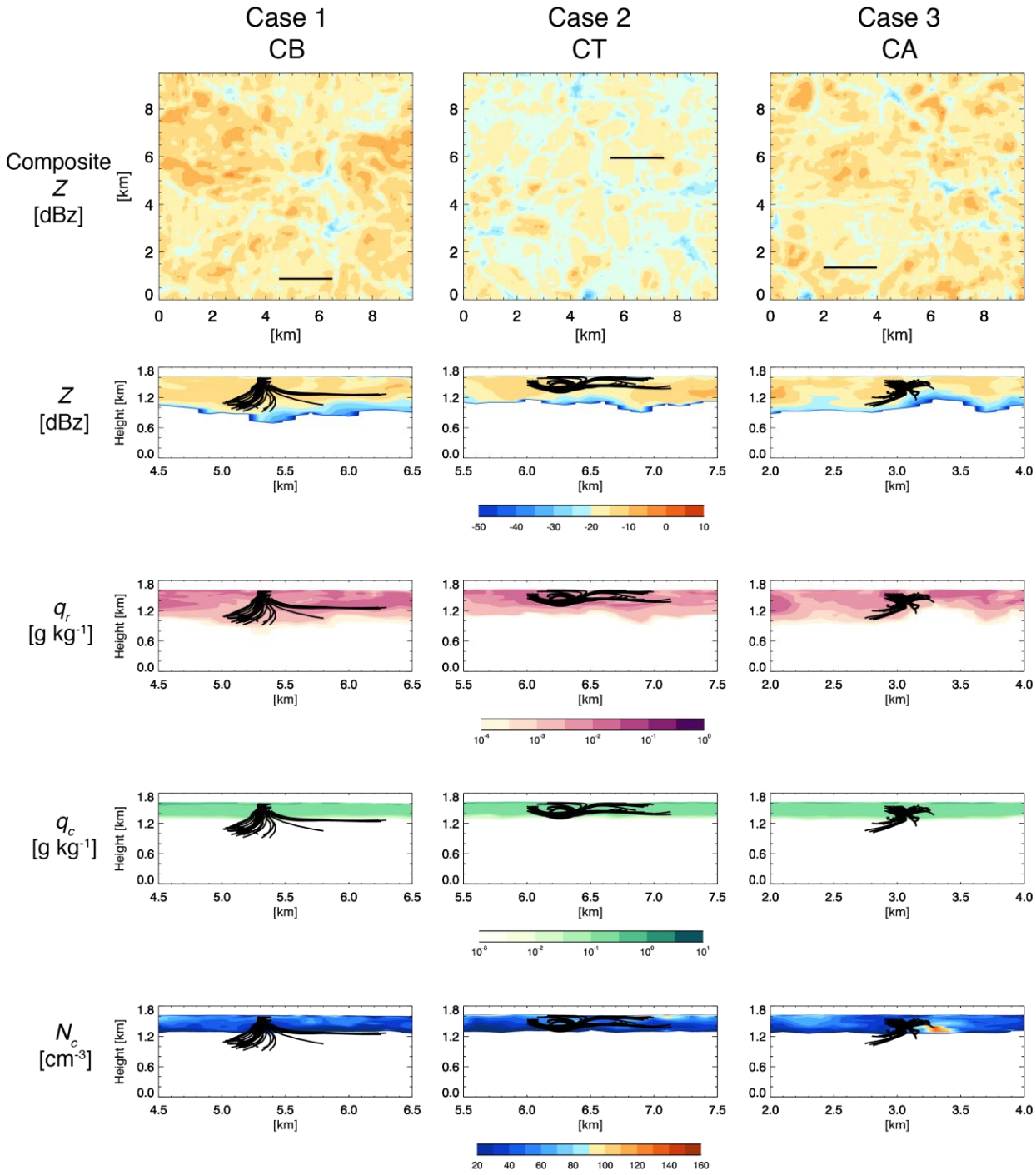

Fig. 8. Composite simulated reflectivity and vertical cross sections of simulated reflectivity, q_r, q_c, and N_c at the trajectory model initialization time and median trajectory initialization location for 3 example cases of characteristic trajectory behavior. 30 trajectory paths are overlayed to show a representation of the characteristic behavior of the trajectories in each case. The cross sections are plotted at the black lines overlayed on composite simulated reflectivity for each case.

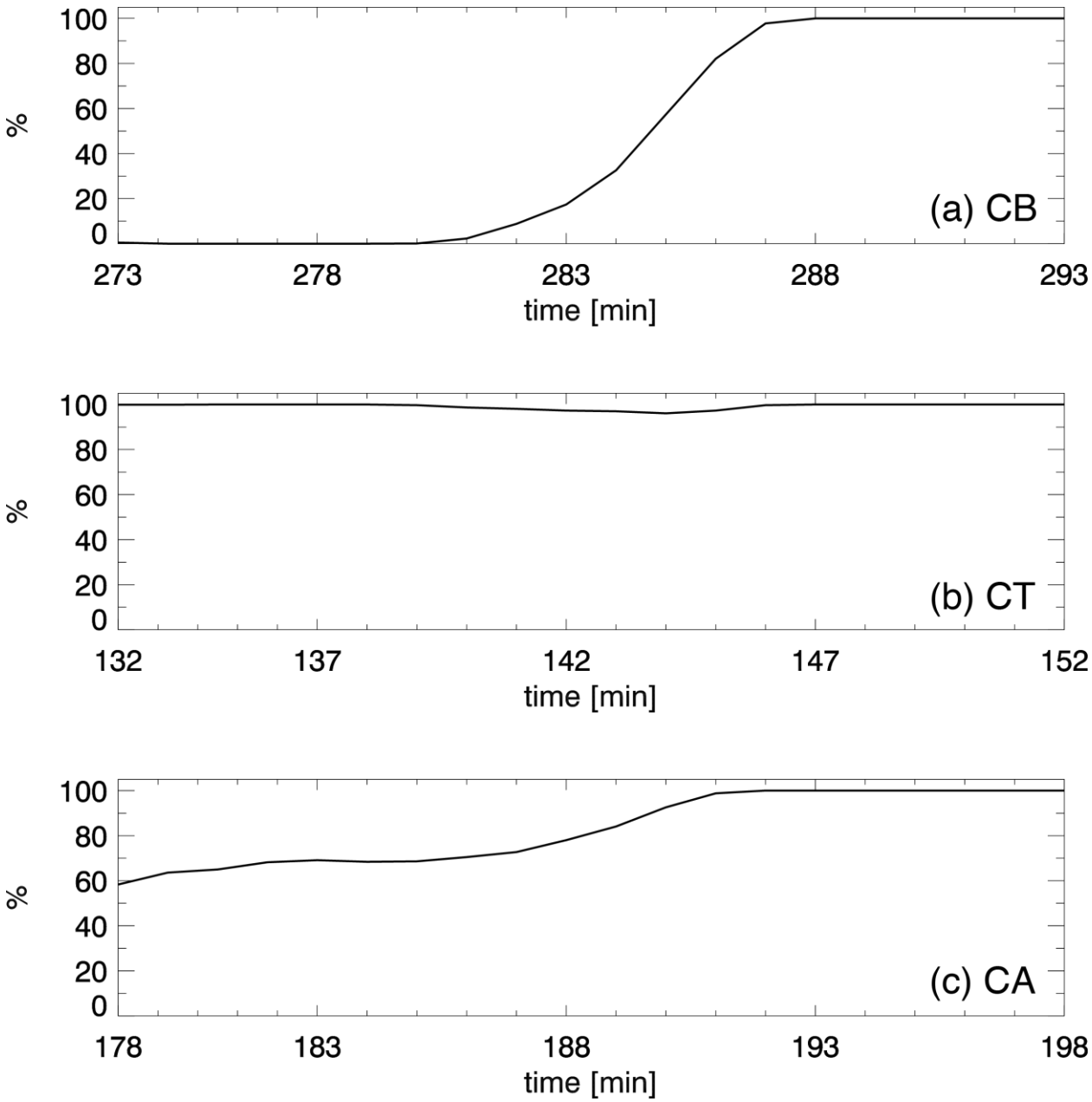

Fig. 9. Time series of the percentage of trajectories located in-cloud for cases (a) CB, (b) CT, and (c) CA. Each time series spans 20 minutes for the length of each trajectory simulation.

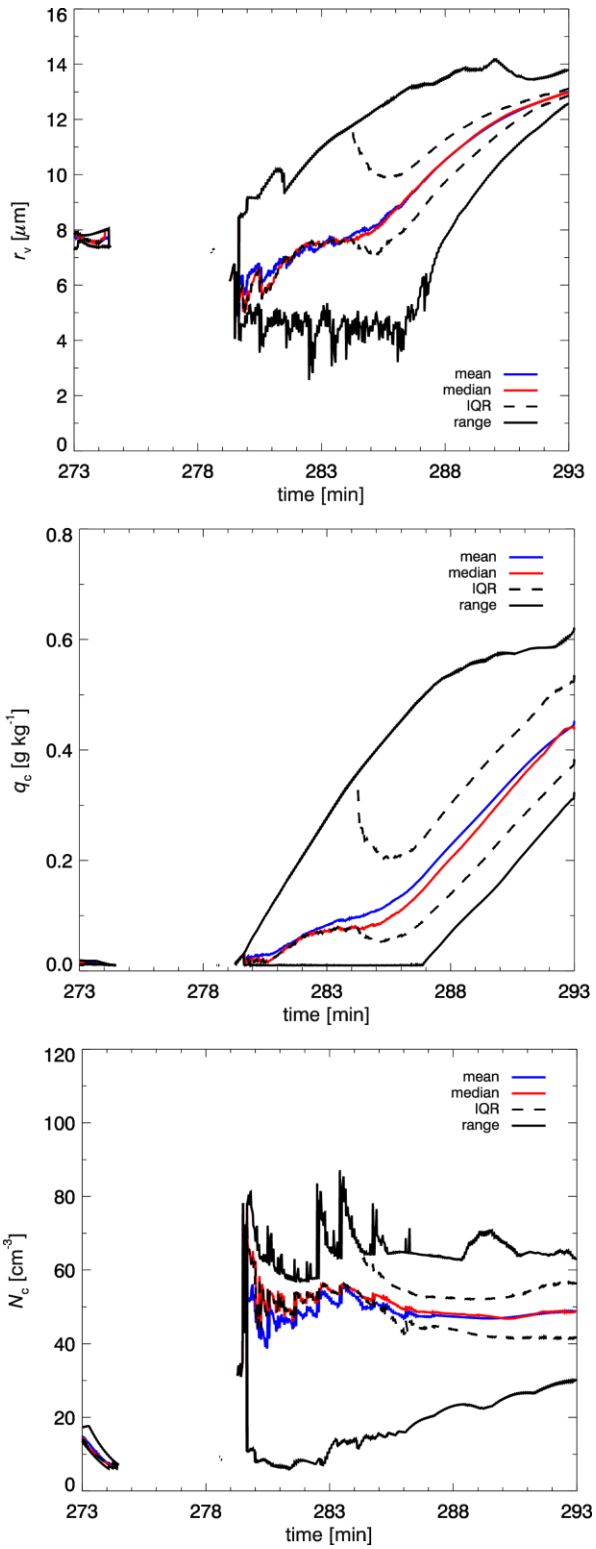

Fig. 10. Time series of in-cloud trajectory mean volume radius of the cloud spectrum r_v, cloud water mixing ratio q_c, and cloud droplet concentration of the cloud spectrum N_c for the example CB case. Each time series spans 20 minutes for the length of each trajectory simulation.

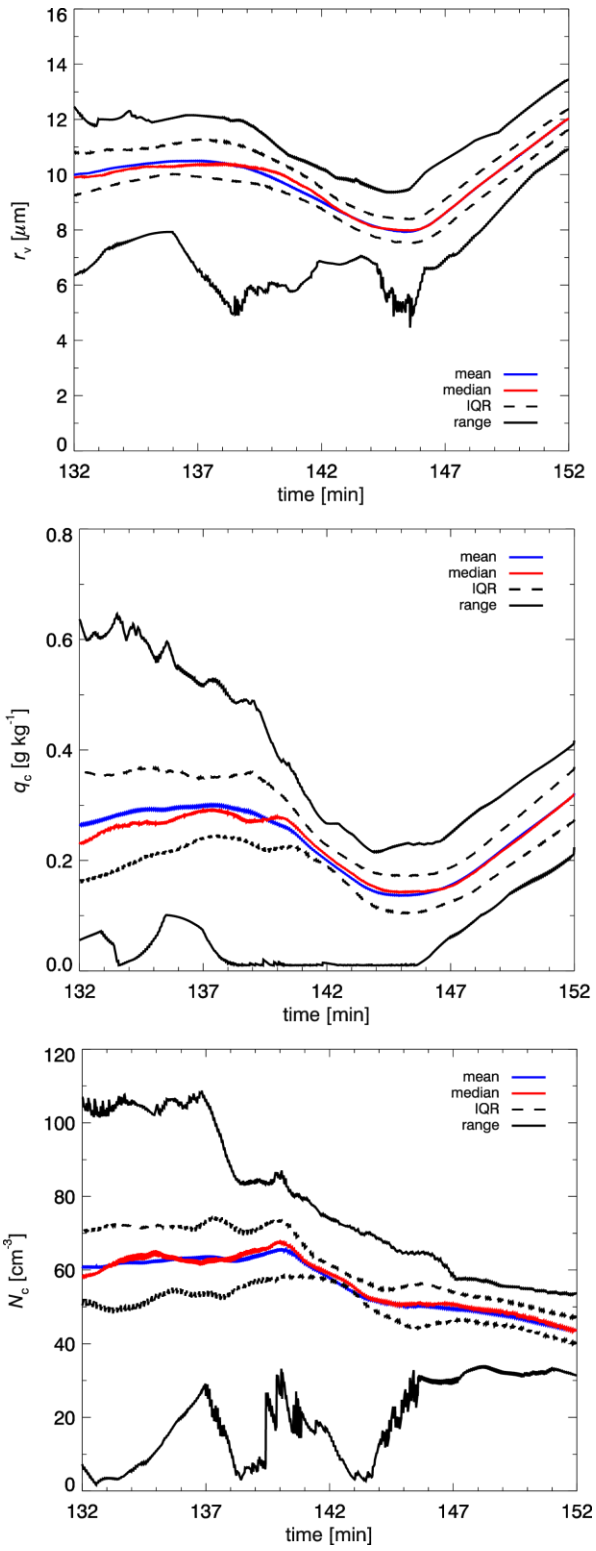

Fig. 11. Same as Fig. 10 except for the example CT case.

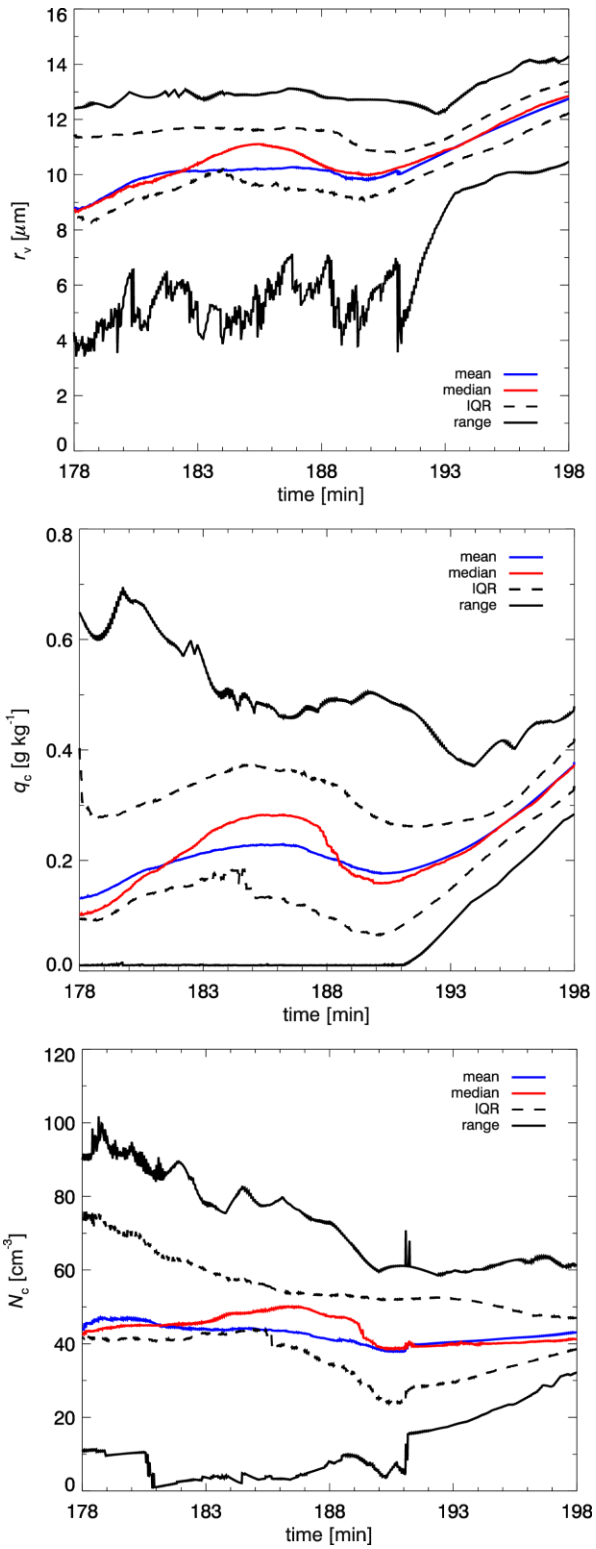

Fig. 12. Same as Fig. 10 except for the example CA case.

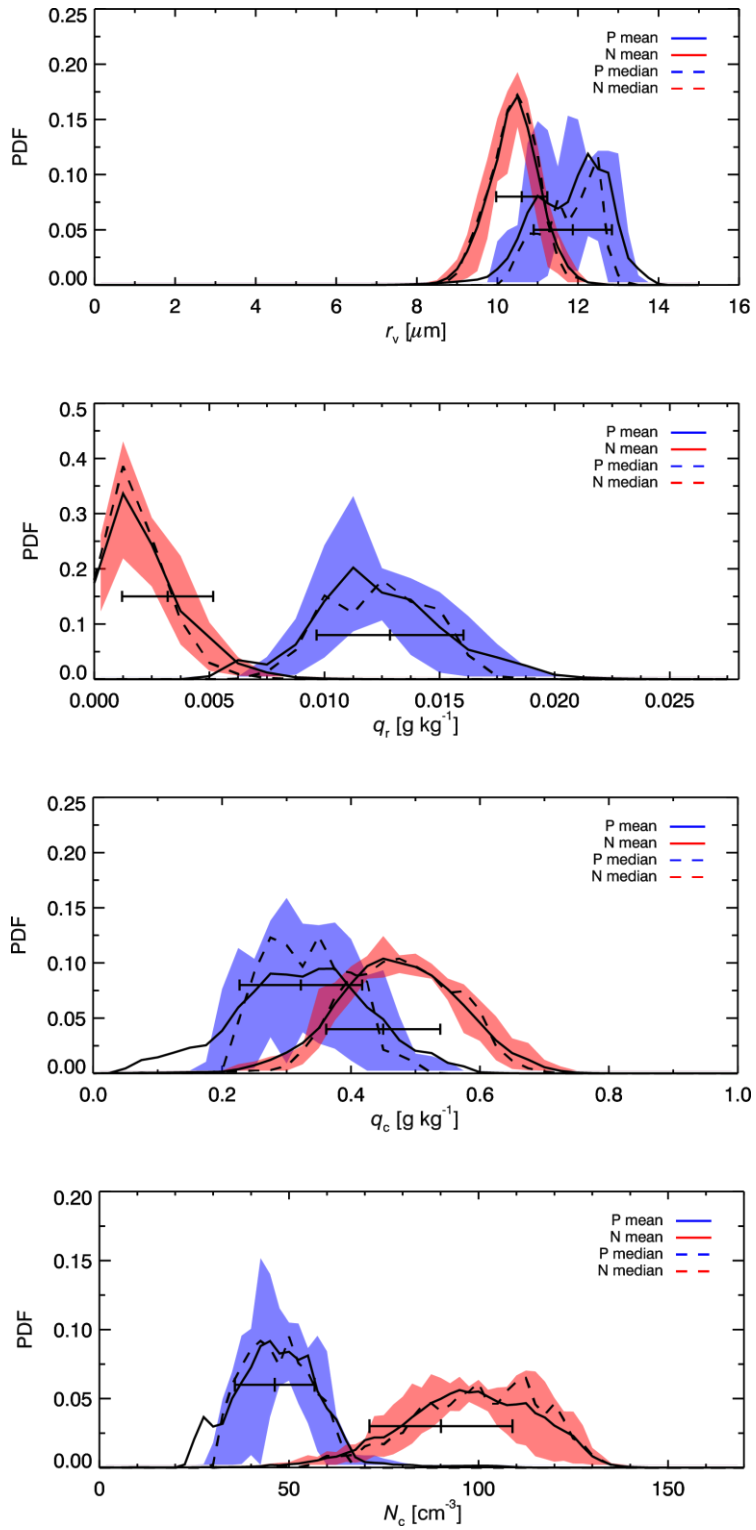

Fig. 13. Normalized averaged frequency distributions (PDFs) of all P and N cases at the last minute of the trajectory simulation for mean volume radius of the cloud spectrum r_v, rain water mixing ratio q_r, cloud water content q_c, and cloud drop concentration of the cloud spectrum N_c. Whiskers represent the mean (middle vertical line) and 1 standard deviation (outside vertical lines).

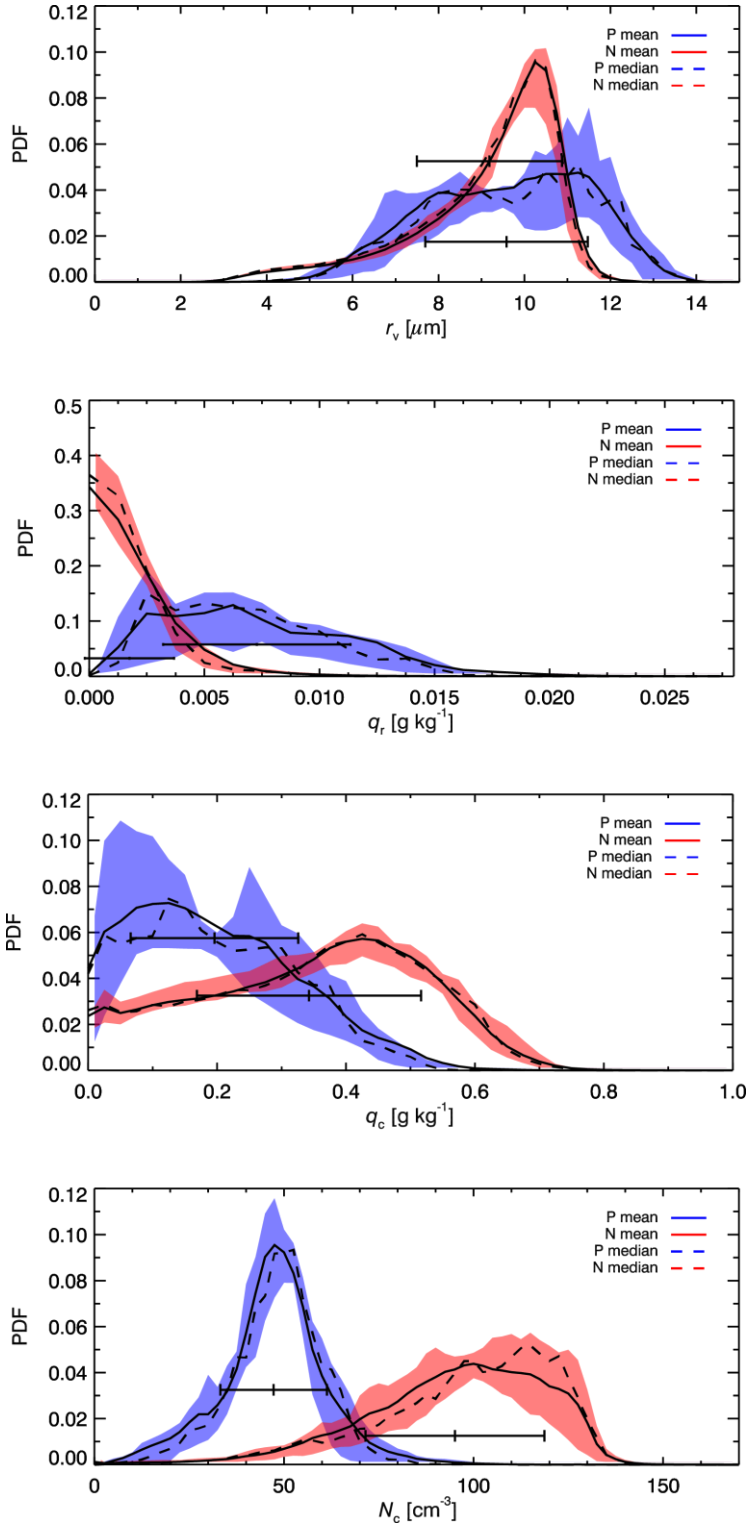

Fig. 14. Same as Fig. 13 except for the entire 20-minute simulation.

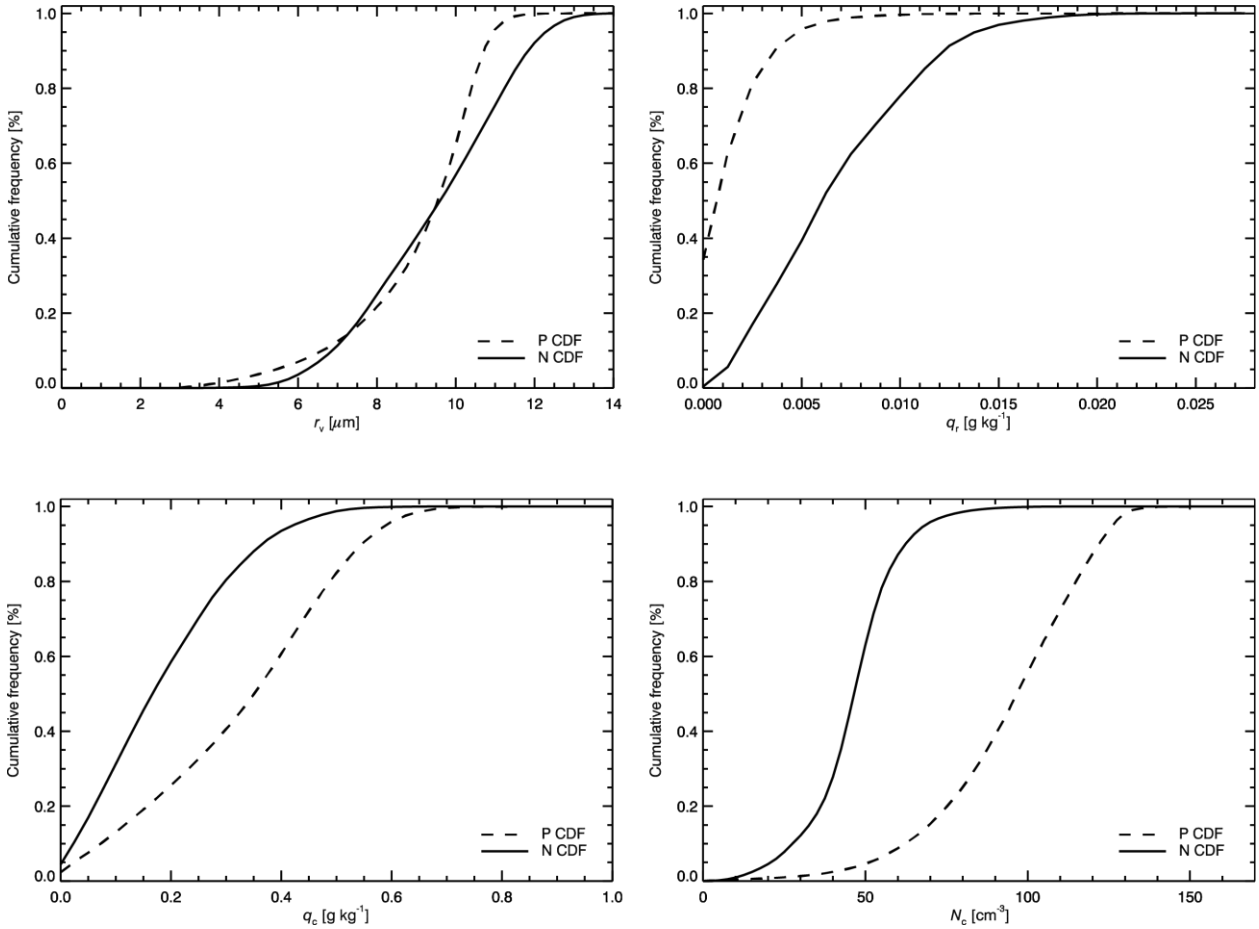

Fig. 15. Averaged cumulative frequency distributions (CDFs) of all P and N cases for the 20-minute trajectory simulation for mean volume radius of the cloud spectrum r_v, rain water mixing ratio q_r, cloud water content q_c, and cloud drop concentration of the cloud spectrum N_c.